

Structural transitions and transport-half-metallic ferromagnetism in LaMnO_3 at elevated pressure

Jiangang He¹, Ming-Xing Chen², Xing-Qiu Chen³, and Cesare Franchini^{1,3*}

¹*Faculty of Physics, University of Vienna and Center for Computational Materials Science, A-1090 Wien, Austria*

²*Faculty of Chemistry, University of Vienna and Center for Computational Materials Science, A-1090 Wien, Austria and*

³*Shenyang National Laboratory for Materials Science, Institute of Metal Research, Chinese Academy of Sciences, Shenyang 110016, China*

(Dated: March 3, 2013)

By means of hybrid density functional theory we investigate the evolution of the structural, electronic and magnetic properties of the colossal magnetoresistance (CMR) parent compound LaMnO_3 under pressure. We predict a transition from a low pressure antiferromagnetic (AFM) insulator to a high pressure ferromagnetic (FM) transport half-metal (tHM), characterized by a large spin polarization ($\approx 80\text{-}90\%$). The FM-tHM transition is associated with a progressive quenching of the cooperative Jahn-Teller (JT) distortions which transform the $Pnma$ orthorhombic phase into a perfect cubic one (through a mixed phase in which JT-distorted and regular MnO_6 octahedra coexist), and with a high-spin ($S = 2$, $m_{Mn} = 3.7 \mu_B$) to low-spin ($S = 1$, $m_{Mn} = 1.7 \mu_B$) magnetic moment collapse. These results interpret the progression of the experimentally observed non-Mott metalization process and open up the possibility of realizing CMR behaviors in a stoichiometric manganite.

PACS numbers: 71.30.+h, 62.50.-p, 75.47.Gk, 72.25.-b

I. INTRODUCTION

Half-metallic ferromagnets (HMFs) are magnetic compounds that are simultaneously metallic and insulator, depending on the spin channel.^{1,2} Their ability to provide fully spin-polarized currents make them ideal candidates for spintronic applications.^{3,4} A prominent class of HMFs is represented by strongly correlated CMR manganites ($\text{La}_{1-x}\text{A}_x\text{MnO}_3$, $\text{A}=\text{Ca}$, Sr , or Ba):⁵ hole-doping LaMnO_3 through the substitution of La with $\text{A}=\text{Ca}$, Sr , or Ba creates itinerant holes that progressively lead to an antiferromagnetic (AFM)-insulator to ferromagnetic (FM)-metal transition and critically determine the coexistence of half-metallic spin imbalance and the so called CMR effect, i.e. a dramatic change of the electrical resistance in the presence of a magnetic field.^{6,7} Soon after the pioneering observation of CMR effect by Jonker and van Santen,⁶ Zener⁸ proposed the double exchange (DEX) mechanism to explain the AFM-insulator ($x = 0$) to FM-metal ($0.2 < x < 0.5$) transition, relying on the O^{2-} -mediated transfer of an electron between inequivalent Mn^{3+} and Mn^{4+} sites. The DEX mechanism qualitatively explained the ferromagnetic interactions and the observed metallic behavior below the Curie temperature T_C , but it turned out to be inadequate to explain the observed high insulating-like resistivity above the transition temperature and, even most importantly, the observation of CMR in stoichiometric phases like $\text{Ti}_2\text{Mn}_2\text{O}_7$.⁹ Conversely, the more recent half-metallic ferromagnetic model,^{10,11} which is based on the spin-polarized calculation of the density of states (DOS) within the Density Functional Theory (DFT), provides several clues to the underlying processes involved in the CMR phenomena and since it does not rely on the mixed-valence (Mn^{3+} and Mn^{4+}) picture it can explain the observation of CMR in stoichiometric phases.⁹

Controlling and understanding CMR-HMFs phenomena in manganites within the DFT framework remains a great challenge because of two fundamental obstacles: (i) strong exchange-correlation effects and the concurrent orbital/lattice/spin correlations which are not well described by conventional DFT methods, and (ii) doping-induced structural disorder, which unavoidably limits the application of quantum mechanical schemes based on repeated unit cells. The drawbacks of DFT in dealing with insulating transition metal oxides can be corrected by employing more sophisticated methods such as hybrid functionals¹² which have been proven to provide substantially improved structural, electronic and magnetic properties,¹³⁻¹⁶ thanks to the inclusion of a portion of exact 'non-local' exchange. Beyond-DFT approaches are particularly necessary to correctly predict structural distortions, magnetic energies and bandgap in LaMnO_3 , which are wrongly described by DFT.^{13,17,18} DFT is unable to describe the JT instabilities, and stabilize a metallic FM solution instead of the experimentally observed JT-distorted AFM insulating state.¹⁸ As for the structural disorder, the possibility to circumvent the problem by realizing CMR-HMF behaviors in stoichiometric samples would represent a substantial benefit not only for theory, but also for the experimental and technological research, thanks to the higher degree of control and manipulability of the relevant physical processes. However the task is hard, and up-to-date very few stoichiometric CMR compounds have been identified.^{9,19}

Boosted by the recent experimental observations of an insulator-to-metal transition (IMT) in dense LaMnO_3 ^{20,22} at about 32 GPa, in this article we explore the structural and magnetoelectric response of LaMnO_3 upon compression up to 150 GPa.

We first recall the basic properties of LaMnO_3 . At zero pressure and low temperature LaMnO_3 is a type-

TABLE I. Structural parameters of LaMnO_3 : low-temperature (4.2 K) experimental data³⁰ versus fully optimized PBE and HSE results with different values of the exact-exchange mixing parameter α : 0 (PBE), 0.10 (HSE-10), 0.15 (HSE-15), 0.25 (HSE-25), and 0.35 (HSE-35). Mn-O_s , Mn-O_m and Mn-O_l , represent the short, medium and long Mn-O bondlengths, whereas $\text{Mn-O}_m\text{-Mn}$ ($^\circ$) and $\text{Mn-O}_{s/l}\text{-Mn}$ ($^\circ$) indicates the corresponding angles. Finally, the JT parameters Q_2 and Q_3 are defined as: $Q_2 = 2(l-s)/\sqrt{2}$ and $Q_3 = 2(2m-l-s)/\sqrt{6}$.

	Exp ^a	HSE-35	HSE-25	HSE-15	HSE-10	PBE
Volume (\AA^3)	243.57	243.98	245.82	247.36	244.24	244.21
a (\AA)	5.532	5.526	5.537	5.553	5.661	5.569
b (\AA)	5.742	5.789	5.817	5.820	5.594	5.627
c (\AA)	7.668	7.628	7.633	7.653	7.712	7.793
Mn-O_m (\AA)	1.957	1.954	1.957	1.962	1.979	1.992
Mn-O_l (\AA)	2.184	2.204	2.214	2.213	2.134	2.063
Mn-O_s (\AA)	1.903	1.899	1.905	1.914	1.923	1.971
$\text{Mn-O}_m\text{-Mn}$ ($^\circ$)	154.3	154.78	154.35	154.36	153.96	155.85
$\text{Mn-O}_{s/l}\text{-Mn}$ ($^\circ$)	156.7	154.38	154.08	154.17	157.59	157.71
Q_2	0.398	0.431	0.437	0.423	0.298	0.131
Q_3	-0.142	-0.159	-0.167	-0.165	-0.080	-0.041

A AFM insulator (alternating planes of similar spins along the c direction) characterized by staggered JT and GdFeO_3 -type (GFO) distortions, manifested by long (l) and short (s) Mn-O in-plane distances and medium (m) Mn-O vertical ones (JT), and by the tilting of the the Mn^{3+}O_6 octahedra (see Fig. 2(d)). These structural instabilities removes the e_g orbital degeneracy and stabilize an orthorhombic high-spin $(t_{2g})^3(e_g)^1$ orbitally ordered configuration.²³ The application of hydrostatic pressure progressively quenches the cooperative JT distortions and leads to an IMT at $P_c=32$ GPa.²⁰ The persistence of the structural distortions up to P_c indicates that the IMT is not a Mott-Hubbard type. This conclusion was initially proposed by LDA+U and Dynamical mean field theory studies^{17,24} and only very recently was confirmed by high pressure Raman measurements.²² Baldini and coworkers²² have also reported the coexistence of domains of distorted and regular octahedra in the pressure range 3-34 GPa, and connected the onset of metallicity with the increase of undistorted MnO_6 octahedra beyond a critical threshold. The concomitant presence of two distinct phases in this pressure range was confirmed by the X-ray absorption spectroscopy experiments of Ramos *et al.*²⁵

Our computational study, beside providing a detailed microscopic understanding of the IMT and of the associated competition between distorted and undistorted phases, predicts that the onset of metallicity is associated with a FM spin transition and that the FM-metal state develops towards a transport half-metal regime at elevated pressure (≈ 100 GPa), where the current is nearly fully spin polarized. Our results are reported and discussed in Sec.III. Before that we describe our computational setup, which is given in Sec.II. Finally, in Sec.IV we draw a summary.

II. METHODOLOGY AND COMPUTATIONAL ASPECTS

All calculations were performed using the the Vienna Ab initio Simulation Package^{26,27} (VASP) within the Heyd, Scuseria, and Ernzerhof (HSE) hybrid density functional scheme,²⁸ in which the exchange-correlation functional is expressed as a suitable admixture of DFT and Hartree-Fock (HF):

$$E_{XC}^{HSE} = \alpha E_X^{HF, sr, \mu} + (1-\alpha) E_X^{PBE, sr, \mu} + E_X^{PBE, lr, \mu} + E_C^{PBE} \quad (1)$$

where $\mu=0.20\text{\AA}-1$, controls the range separation between the short-range (sr) and long-range (lr) part of the Coulomb kernel, and α determines the fraction of exact HF exchange incorporated. The parameter α , which we set equal to 0.15, is chosen so as to provide accurate values for the band gap, structural distortions and magnetic energies, as discussed below.

We have used a computational unit cell containing four LaMnO_3 formula units (i.e. 20 atoms) to simulate both the P_{nma} and simple-cubic phase within the ferromagnetic (FM) and type-A AFM orderings. Convergence tests on the energy cut-off has shown that at low and intermediate pressure range the energy difference ΔE between the FM and AFM phases (our most critical quantity) changes by less than 3 meV per formula unit (f.u.) when the energy cut-off is increased from 300 meV to 400 meV. We have therefore chosen the value 300 meV, and made use of a $4\times 4\times 4$ Monkhorst-Pack k-point grid for both the exchange-correlation DFT kernel and the portion ($\alpha=0.15$) of exact HF exchange.

We have used the following structural optimization procedure. For each volume we have fully relaxed the cell shape (i.e., lattice parameters a , b , and c as well as the corresponding angles between them) and all internal

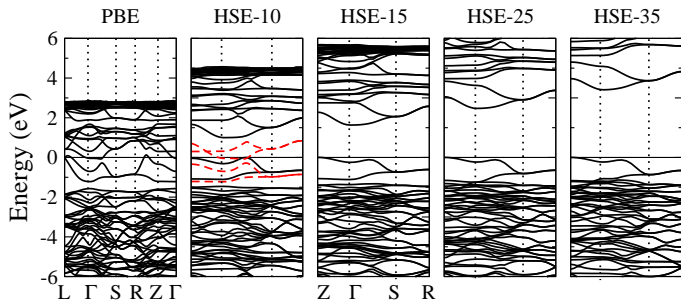


FIG. 1. (Color online) PBE & HSE band structure of LaMnO_3 along the $\text{Z}\Gamma\text{SR}$ (HSE) and $\text{L}\Gamma\text{SRZ}\Gamma$ (PBE) obtained using different values of the mixing parameter at the corresponding optimized geometry. The Fermi level is set to zero. For PBE we have included more high-symmetry lines in order to show that both e_g bands above and below E_F cross the Fermi level. The PBE bands along the $\text{Z}\Gamma\text{SR}$ are shown as (red) dashed lines in panel HSE-10.

structural degrees of freedom (all atomic positions). This complete geometrical optimization allowed us to tread the structural path from the P_{nma} to the cubic phases. We have tested about 30 different volumes. The equation of states (Pressure-Volume curves) were calculated in two different ways: (i) by computing the pressure directly from the stress tensor (as automatically done by VASP) and (ii) by applying the Birch-Murnaghan equation.²⁹ Both routes lead to the same result.

TABLE II. The band gap (Δ , eV), magnetic moment (m , μ_B/Mn), and relative energy with respect to the FM ordering calculated by HSE for different values of the mixing parameter α .

	Expt.	HSE-35	HSE-25	HSE-15	HSE-10	PBE
Δ	1.1 ^a , 1.7 ^b	3.41	2.47	1.45	0.75	0.00
m	3.7 ^c	3.78	3.74	3.67	3.65	3.52
A-AFM		-7	-8	-24	3	171
C-AFM		156	182	198	368	564
G-AFM		161	192	208	428	899

^aRef.,³¹ ^bRef.,³² ^cRef.³⁰

A. Choice of the mixing factor α : ground state properties of LaMnO_3

In order to determine the HSE mixing factor α , i.e. the fraction of non-local HF exchange included in the hybrid exchange-correlation functional, we have performed a set of calculations of the ground state structural, electronic and magnetic properties of LaMnO_3 for different values of α : 0 (corresponding to a purely PBE setup), 0.10 (HSE-10), 0.15 (HSE-15), 0.25 (HSE-25) and 0.35 (HSE-35).

The results, collected in Tab.I (optimized geometry) and Tab.II (bandgap, magnetic moment and magnetic energies), demonstrate that the best choice is $\alpha=0.15$. For this value of the mixing parameter HSE delivers (see Tab.I and Tab.II) (i) an insulating bandgap, $\Delta=1.45$, well within the measured data, (ii) a correct description of the critical cooperative Jahn-Teller (JT) parameters Q_2 and Q_3 , and (iii) a AFM magnetic ground state in agreement with the experimental findings. Smaller mixing factors (0 and 0.10) lead to a significant underestimation of the JT parameters Q_2 and Q_3 (see Tab.I) and to a much too small bandgap (which is actually zero in PBE, see Tab.II), and to the stabilization of the FM spin arrangement (see Tab.II), in contrast to the experimental situation. This is in line with previous conventional DFT studies.^{18,33–35} We note that by using the experimental structure a small bandgap of about 0.2 eV is opened at PBE level, which is still too small as compared to the measured level. Conversely, an higher α (0.25 and 0.35) correctly favors the AFM ordering but overestimates the band gap (2.47 and 3.41 for $\alpha=0.25$ and $\alpha=0.35$, respectively). The value of the gap obtained for $\alpha=0.25$ is very similar to the corresponding B3LYP value, 2.3 eV,¹³ and to the HSE value obtained using the experimental structure, 2.25 eV.³⁶

In terms of the band dispersions the effect of the mixing parameter is the progressively larger separation of the occupied and unoccupied e_g bands below and above the Fermi energy with increasing α , as shown in Fig. 1, but qualitatively the overall bonding picture remains unchanged. In contrast, in PBE the e_g sub-bands cross the Fermi Energy and form a spurious metallic solution.

III. RESULTS AND DISCUSSION

The progression of the structural properties of compressed LaMnO_3 computed by HSE as a function of $v=V/V_0$ is summarized in Fig. 2, whereas the corresponding development of the electronic and magnetic properties is shown in Figs. 3, 5 and 6. In the pressure range 0-35 GPa, for which experimental data are available, our results are in very good agreement with measurements in terms of: (i) the pressure-volume equation of states and bulk modulus B_0 ($B_0^{\text{Expt}}=108$ GPa, $B_0^{\text{HSE}}=104$ GPa, see Fig. 2(a)), (ii) the pressure-induced changes in the structural parameters (Fig. 2(b)), and (iii) the concurrent suppression of the JT modes Q_2 and Q_3 and the band gap at the same compression ($v_2=0.82$, slightly smaller than the experimental one, $V/V_0=0.86$, see Fig. 2(b) and Fig. 3(a)); the $P=0$ HSE gap opened between occupied and empty e_g states, $E_g=1.45$ eV (Fig. 3(c)), is well within the measured range, 1.1-1.7 eV.^{31,32} Similarly the HSE ground state values of Q_2 and Q_3 match exactly the experimental values.³⁰

The incremental compression of LaMnO_3 leads to a continuous structural transformation from the $P=0$ dis-

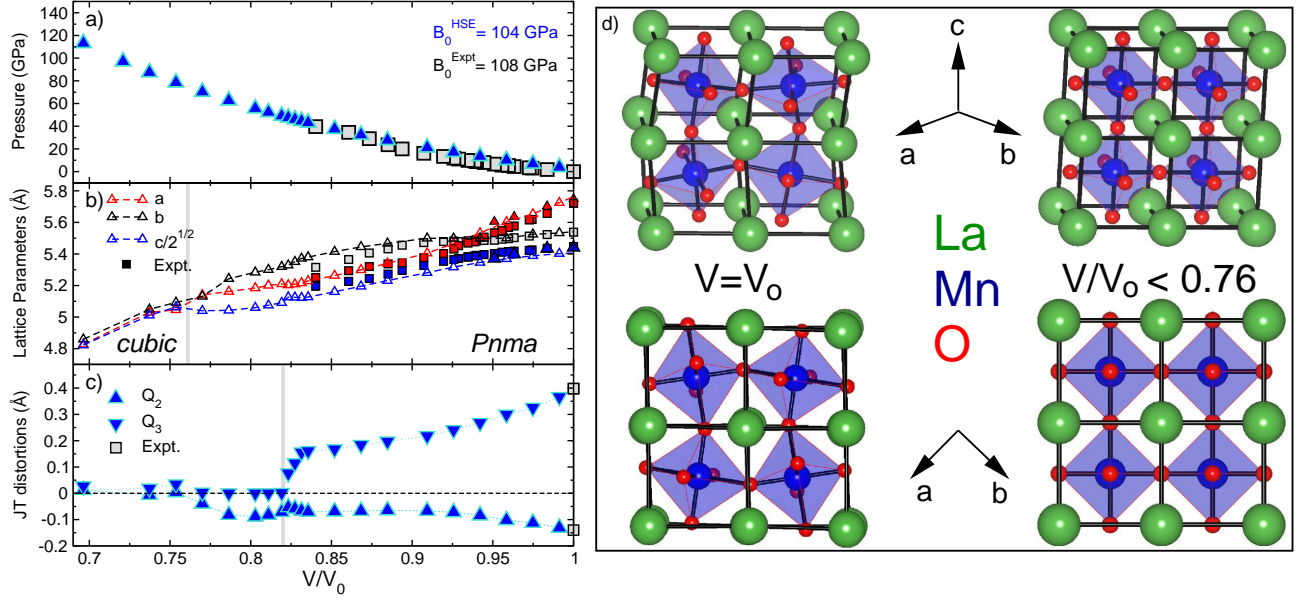


FIG. 2. (Color online) Evolution of the structural properties of LaMnO_3 as a function of $v=V/V_0$ as predicted by HSE (triangles) and compared with the experimental data (squares) taken from Refs. 20, 21, and 30. (a) Equation of state (the inset indicates the value of the bulk modulus); (b) Structural parameters: at $v_3=0.76$ LaMnO_3 undergoes an orthorhombic ($a \neq b \neq \sqrt{c/2}$) to cubic ($a = b = \sqrt{c/2}$) transition marked by the vertical line. (c) Progressive quenching of the cooperative Jahn-Teller local modes $Q_2 = 2(l-s)/\sqrt{2}$ and $Q_3 = 2(2m-l-s)/\sqrt{6}$ with increasing pressure, where l , s and m indicate the long, short and medium Mn-O bondlength; the JT modes are almost completely quenched at the onset of metallicity, marked by the vertical line at $v_2=0.82$ (see Fig. 3); (d) Side (top) and top (bottom) view of the $Pnma$ (left, $V/V_0=1$) and cubic (right, $V/V_0 < 0.76$) phases of LaMnO_3 , underlining the suppression of the JT and GFO structural distortion in the perfect cubic phase.

torted $Pnma$ phase to a perfect cubic structure via a gradual quenching of the JT modes, the rectification of the GFO tilting angles and the alignment of the a , b , and c lattice parameters towards the same value, ≈ 5.1 Å at $v_3=0.76$ as outlined in Fig.2(b-d). The e_g bands around the Fermi energy (E_F) come progressively closer until the gap is closed (Fig.3(c-f)). Concomitantly, the unoccupied t_{2g} bands is pushed down in energy and ultimately crosses the E_F at $v_2=0.82$, the onset of metallicity (see Fig. 3(f)). At this critical volume HSE predicts a jump in the relative stability between the AFM and FM ordering, with the latter becoming the most favorable one by about 90 meV/f.u., as illustrated in Fig. 3(b). At low/intermediate compressions ($V/V_0 > v_2=0.82$) the data displayed in Fig.3(b) shows a strong competition between the AFM and FM phases. HSE predicts a crossover between the AFM and FM phases at $v_1=0.95$ (corresponding to a pressure of 11 GPa), below which the AFM and FM ordering become almost degenerate ($\Delta E < 12$ meV/f.u.). Considering that in the FM phase the JT/GFO distortions are almost completely inhibited (see Fig. 4), this result strongly supports the latest Raman²² and X-ray absorption spectroscopy²⁵ studies reporting the formation of a mixed state of domains of distorted and regular MnO_6 octahedra in the range 13–34 GPa, which compare well with the corresponding theoretical pressure range, 11–

50 GPa ($v_2 < V/V_0 < v_1$). The coexistence of distorted and undistorted octahedra is clarified in Fig. 4 where we plot the comparison between the evolution of the JT distortions in the FM and AFM phases (panel (a)), and the energy-volume phase diagram (panel (b)). In the FM phase the Q_2 and Q_3 drop down to zero at about 11 GPa ($V/V_0=v_1=0.95$), indicating that for pressure larger than 11 GPa the MnO_6 octahedra are undistorted. Conversely, as already underlined, in the AFM phase the octahedra remain distorted until $V/V_0=v_2=0.82$ (about 50 GPa). This different behaviour is interpreted graphically in the insets of Fig. 4(a) which represents the FM-undistorted (u) and AFM-distorted (d) octahedra. Summing up, at low/high pressures LaMnO_3 is AFM-distorted/FM-undistorted, whereas in the volume range $v_2 < V/V_0 < v_1$ these two phases coexist in a mixed domains of distorted and undistorted octahedra (see Fig. 4(b)).

The FM transition at $V/V_0=0.82$ comes right before an high spin (HS, $S=2$) to low spin (LS, $S=1$) moment collapse, which is correlated with the e_g and t_{2g} orbital occupations as shown in Fig. 6: under compression the Mn^{3+} ion retains its $P=0$ ($t_{2g})^{\uparrow\uparrow\uparrow}(e_g)^{\uparrow}$ orbital configuration down to $V/V_0=0.80$, with a magnetic moment of $3.7 \mu_B$; further compression yields a rapid reduction of the magnetic moment down to $1.7 \mu_B$, due the redistribution of electrons within the $3d$ shell which ultimately leads to

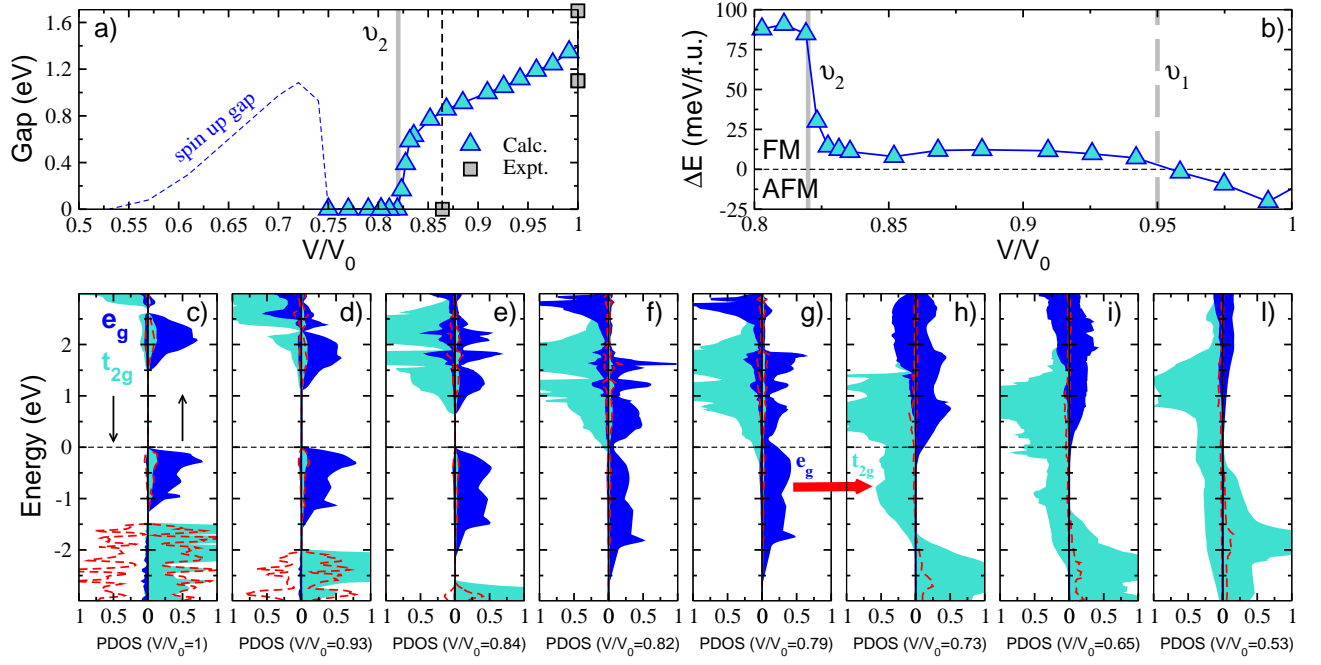


FIG. 3. (Color online) Evolution of the calculated electronic properties and magnetic ordering of LaMnO_3 upon pressure. (a) Band gap: IMT at $\nu_2=0.82$ (marked by the vertical full line; the dashed line refers to the corresponding experimental onset). Measured gaps are taken from Ref..^{31,32} (b) Energy difference ΔE between the AFM and FM spin arrangements: AFM/FM crossover at $\nu_1=0.95$ (indicated by a vertical dashed line) and stabilization of the FM state at $\nu_2=0.82$. (c-l) Changes in the e_g and t_{2g} density of states around the Fermi level with pressure. The dashed (red) lines refer to the Oxygen p states, whereas the thick (red) arrow indicates the transfer of one electron from the e_g to the t_{2g} sub-bands.

the low-spin configuration $(t_{2g})^{\uparrow\uparrow\downarrow}(e_g)^0$. The HS-to-LS collapse starts to develop at about $V/V_0=0.8$ and is fully established at exactly the same volume at which the cubic phase emerges, $\nu_3=0.76$. This HS-orthorhombic to LS-cubic transition is also reflected in the DOS (Fig. 3 (g-i)), whose evolution from $V/V_0=0.79$ to $V/V_0=0.73$ clearly indicates the transfer of one electron from the e_g to the t_{2g} sub-bands and the subsequent realization of a nearly FM half-metallic state with a metallic minority t_{2g} band and a quasi-insulating majority channel with a residual density of e_g electrons at the bottom of the conduction band. In order to clarify further the HS-to-LS transition we display in Fig. 5 the partial and integrated density of states in a wide energy windows associated with the e_g and t_{2g} bands at $V/V_0=0.79$ and $V/V_0=0.73$, which show the transfer of one electron from the e_g spin up channel at $V/V_0=0.79$ to the t_{2g} spin-down channel at $V/V_0=0.73$, which yields to the $(t_{2g})^{\uparrow\uparrow\downarrow}(e_g)^{\uparrow}$ to $(t_{2g})^{\uparrow\uparrow\downarrow}(e_g)^0$ transition.

Following the classical work of Nadgorny *et al.*¹⁰ we have analyzed the spin polarization P_n associated to this high pressure nearly HM-FM state in order to acquire information on the spin-dependent transport properties, using the formula suggested by Mazin:³⁸

$$P_n = \frac{N_{\uparrow}(E_F)v_{F\uparrow}^n - N_{\downarrow}(E_F)v_{F\downarrow}^n}{N_{\uparrow}(E_F)v_{F\uparrow}^n + N_{\downarrow}(E_F)v_{F\downarrow}^n} \quad (2)$$

where $N_{\uparrow}(E_F)$, $N_{\downarrow}(E_F)$ and $v_{F\uparrow}$, $v_{F\downarrow}$ represent the ma-

jority and minority spin DOS and Fermi velocities, respectively, and the index n refers to the different types of spin polarizations detected in spin-resolved photoemission measurements ($n = 0$), and in ballistic ($n = 1$) and diffusive ($n = 2$) transport experiments. We have computed the Fermi velocities by interfacing the VASP with the BoltzTrap code,³⁹ and obtained for $V/V_0=0.70$: $P_0 = 87\%$, $P_1 = 80.5\%$, and $P_2 = 71\%$, and for $V/V_0=0.65$: $P_0 = 92\%$, $P_1 = 87\%$ and $P_2 = 80\%$, values very similar to those reported for the doped CMR manganite $\text{La}_{0.7}\text{Sr}_{0.3}\text{MnO}_3$.¹⁰ We can thus conclude, that the high pressure FM cubic phase of LaMnO_3 is a *transport* half-metal. For denser phases ($V/V_0 < 0.65$) the majority spin band gap (from the lower laying filled t_{2g} and the unoccupied e_g band) is progressively reduced to zero at $V/V_0 < 0.53$ ($P > 300$ GPa, see Fig.3(a)). Being the FM-tHM regime the crucial common ingredient of all CMR manganites, its realization in the undoped (stoichiometric) phase of the CMR parent compound LaMnO_3 in a wide interval of compressions, could help in achieving new fundamental insights into the elusive phenomena of CMR.

IV. SUMMARY

Summarizing, we have traced the development of LaMnO_3 upon pressure and determined a sequence of

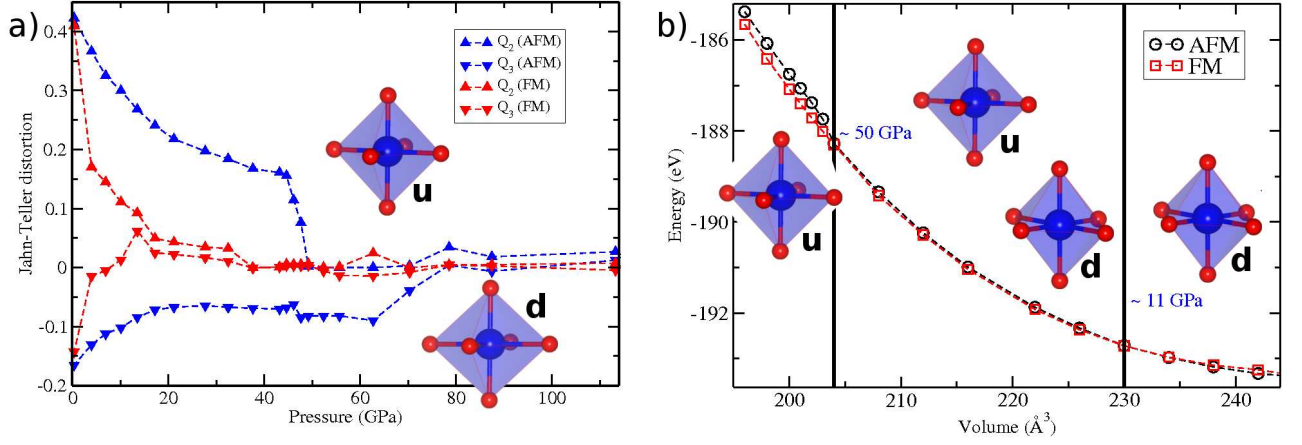


FIG. 4. (Color online) (a) Development of the JT quantities Q_1 and Q_2 upon pressure for the FM and AFM ordering. (b) Energy-Volume curve showing the coexistence of JT-distorted and undistorted phases in the volume range $v_2[V/V_0]v_1$. This volume region is delimited by the vertical lines. In both panels the insets represent FM-undistorted (u) and AFM-distorted (d) MnO₆ octahedra.

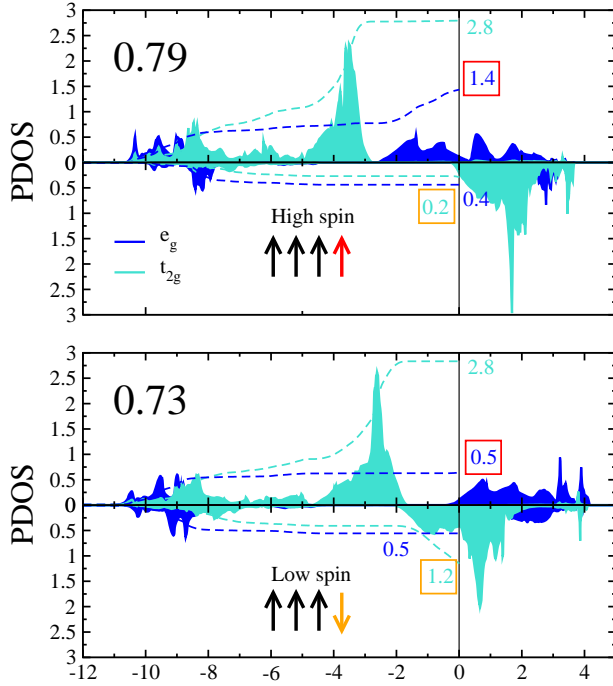


FIG. 5. (Color online) Partial and integrated density of states of LaMnO₃ at $V/V_0=0.79$ and $V/V_0=0.73$ representing the pressure induced High-Spin to Low-Spin transition and associated $e_g^\uparrow(V/V_0=0.79) \rightarrow t_{2g}^\downarrow(V/V_0=0.73)$ electron transfer. The arrows indicate the HS and LS configuration at $V/V_0=0.79$ and $V/V_0=0.73$, respectively, whereas the small numbers represent the number of electrons for the specific lm -channel (those in squares are those involved in the electron transfer).

highly interconnected structural, electronic, and magnetic phase transitions: (i) At ambient conditions LaMnO₃ possesses a distorted AFM insulating state. At $v_1=0.95$ a competition between (distorted) AFM and

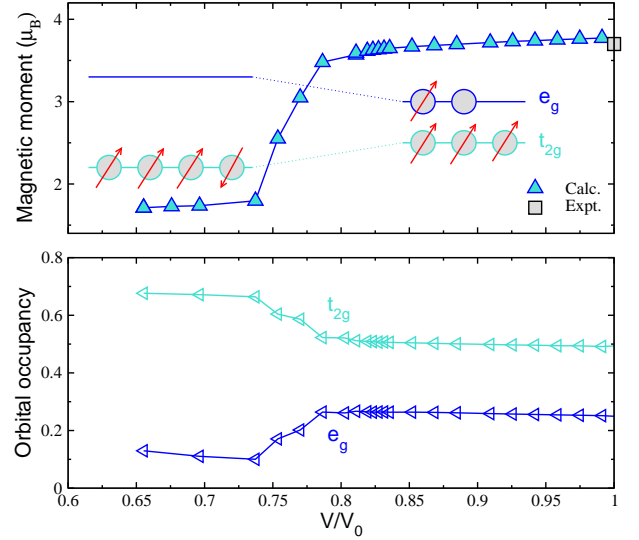


FIG. 6. (Color online) (a) Pressure driven magnetic moment collapse and corresponding correlation with (b) the e_g and t_{2g} orbital occupancy. The insets in panel (a) illustrate the schematic diagrams of the HS and LS states at low (right) and high (left) pressure. The square indicates the experimental magnetic moment at ambient pressure taken from Ref.³⁰ A similar transition has been observed in dense MnO.³⁷

(undistorted) FM configuration begin to evolve. (ii) At the critical threshold $v_2=0.82$ LaMnO₃ undergoes a non-Mott IMT associated with a significant reduction of the JT/GFO instabilities. (iii) For $v_3=0.76$ all residual lattice distortions are suppressed and a perfect cubic phase emerges. (iv) At $v_4=0.70$ the strong crystal field splitting between t_{2g} and e_g drives a magnetic moment collapse from an HS to LS tHM-FM state, manifested by a significant disproportionation in the spin-dependent $N(E_F)$, v_F , and consequentially P_n . Our results, thus, predict

that it is possible to establish a tHM-FM regime in a stoichiometric manganite at pressure accessible by high-pressure technology.

ACKNOWLEDGEMENTS

Support by European Community (FP7 grant ATHENA), the Chinese Academy of Science (CAS Fel-

lowship for Young International Scientists) and the National Science Foundation of China (NSFC Grand 51050110444) is gratefully acknowledged. X.-Q.C is grateful for supports from the CAS Hundred Talents Project and from NSFC of China (Grand Numbers: 51074151 and 51174188). All calculations have been performed on the Vienna Scientific Cluster.

-
- * Corresponding author: cesare.franchini@univie.ac.at
- ¹ R. A. de Groot, F. M. Mueller, P. G. van Engen, and K. H. J. Buschow, *Phys. Rev. Lett.* **50** 2024 (1983).
 - ² M. I. Katsnelson, V. Yu. Irkhin, L. Chioncel, A. I. Lichtenstein, R. A. de Groot, *Rev. Mod. Phys.* **80**, 315 (2008).
 - ³ I. Žutić, J. Fabian, and S. Das Sarma, *Rev. Mod. Phys.* **76**, 323 (2004).
 - ⁴ G. A. Prinz, *Science* **282** 1660 (1998).
 - ⁵ J.M.D. Coey, M. Viret and S. von Molnár, *Adv. in Phys.* **48**, 167 (1999).
 - ⁶ G. H. Jonker and J. H. van Santen, *Physica* **16**, 337 (1950).
 - ⁷ M. B. Salamon and M. Jaime, *Rev. Mod. Phys.* **73**, 583 (2001).
 - ⁸ C. Zener, *Phys. Rev.* **82**, 403 (1951).
 - ⁹ Y. Shimakawa, Y. Kubo, and T. Manako, *Nature* **379**, 53 (1996).
 - ¹⁰ B. Nadgorny, I. I. Mazin, M. Osofsky, R. J. Soulen, Jr., P. Broussard, R. M. Stroud, D. J. Singh, V. G. Harris, A. Arsenov, and Ya. Mukovskii, *Phys. Rev. B* **63**, 184433 (2001).
 - ¹¹ W. E. Pickett and D. J. Singh, *Phys. Rev. B* **53**, 1146 (1996).
 - ¹² A.D. Becke, *J. Chem. Phys.* **98** 1372 (1993).
 - ¹³ D. Muñoz, N. M. Harrison, and F. Illas, *Phys. Rev. B* **69**, 085115 (2004).
 - ¹⁴ T. Archer, C.D. Pemmaraju, S. Sanvito, C. Franchini, J. He, A. Filippetti, P. Delugas, D. Puggioni, V. Fiorentini, R. Tiwari and P. Majumdar, *Phys. Rev. B* **84**, 115114 (2011).
 - ¹⁵ C. Franchini, A. Sanna, M. Marsman, G. Kresse, *Phys. Rev. B* **81**, 085213 (2010).
 - ¹⁶ C. Franchini, T. Archer, Jiangang He, Xing-Qiu Chen, A. Filippetti, S. Sanvito, *Phys. Rev. B* **83**, 220402(R) (2011).
 - ¹⁷ G. Trimarchi and N. Binggeli, *Phys. Rev. B* **71**, 035101 (2005).
 - ¹⁸ T. Hashimoto, S. Ishibashi, and K. Terakura, *Phys. Rev. B* **82**, 045124 (2010).
 - ¹⁹ S. Ishiwata, T. Nakano, I. Terasaki, H. Nakao, Y. Murakami, Y. Uwatoko, and M. Takano, *Phys. Rev. B* **83**, 020401(R) (2011).
 - ²⁰ I. Loa, P. Adler, A. Grzechnik, K. Syassen, U. Schwarz, M. Hanfland, G. Kh. Rozenberg, P. Gorodetsky, and M. P. Pasternak, *Phys. Rev. Lett.* **87** 125501 (2001).
 - ²¹ L. Pinsard-Gaudart, J. Rodríguez-Carvajal, A. Daoud-Aladine, I. Goncharenko, M. Medarde, R. I. Smith, and A. Revcolevschi, *Phys. Rev. B* **64**, 064426 (2001).
 - ²² M. Baldini, V. V. Struzhkin, A. F. Goncharov, P. Postorino, and W. L. Mao, *Phys. Rev. Lett.* **106** 066402 (2011).
 - ²³ Y. Murakami, J. P. Hill, D. Gibbs, M. Blume, I. Koyama, M. Tanaka, H. Kawata, T. Arima, Y. Tokura, K. Hirota, and Y. Endoh, *Phys. Rev. Lett.* **81**, 582 (1998).
 - ²⁴ A. Yamasaki, M. Feldbacher, Y.F. Yang, O.K. Andersen, K. Held, *Phys. Rev. Lett.* **96**, 166401 (2006).
 - ²⁵ A.Y. Ramos, N. M. Souza-Neto, H. C. N. Tolentino, O. Bunau, Y. Joly, S. Grenier, J.-P. Itié, A.-M. Flank, P. Lagarde and A. Caneiro, *Europhys. Lett.* **96** 36002 (2011).
 - ²⁶ G. Kresse and J. Furthmüller, *Comput. Mat. Sci.* **6**, 15 (1996).
 - ²⁷ G. Kresse and D. Joubert, *Phys. Rev. B*, **59**, 1758 (1999).
 - ²⁸ J. Heyd, G. E. Scuseria, and M. Ernzerhof, *J. Chem. Phys.* **118**, 8207 (2003); Erratum: *J. Chem. Phys.* **124**, 219906 (2006).
 - ²⁹ Francis Birch, *Phys. Rev.* **71** 809 (1947).
 - ³⁰ J.B.A.A. Elemans, B. van Laar, K.R. van der Veen, and B.O. Loopstra, *J. Phys. Chem. Solids* **3**, 238 (1971).
 - ³¹ T. Arima, Y. Tokura, and J.B. Torrance, *Phys. Rev. B* **48** 17006 (1993).
 - ³² T. Saitoh, A. E. Bocquet, T. Mizokawa, H. Namatame, A. Fujimori, M. Abbate, Y. Takura, M. Takano, *Phys. Rev. B* **51**, 13942 (1995).
 - ³³ H. Sawada, Y. Morikawa and K. Terakura, N. Hamada, *Phys. Rev. B* **56**, 12154 (1997).
 - ³⁴ H. Sawada and K. Terakura, *Phys. Rev. B* **58**, 6831 (1998).
 - ³⁵ E. A. Kotomin, R. A. Evarestov, Yu. A. Mastrikov and J. Maier, *Phys. Chem. Chem. Phys.* **7**, 2346 (2005).
 - ³⁶ C. Franchini, R. Kováčik, M. Marsman, S. Sathyanarayana Murthy, J. He, C. Ederer, and G. Kresse, arXiv:1111.1528 (2011).
 - ³⁷ J. Kuneš, Alexey V. Lukoyanov, Vladimir I. Anisimov, Richard T. Scalettar and Warren E. Pickett, *Nat. Mat.* **7**, 198 (2008).
 - ³⁸ I.I. Mazin, *Phys. Rev. Lett.* **83**, 1427 (1999).
 - ³⁹ G.K.H. Madsen and D.J. Singh, *Comput. Phys. Commun.* **67** 175 (2006).